Catalysis Science & Technology

ROYAL SOCIETY OF CHEMISTRY

PAPER

View Article Online
View Journal | View Issue

Check for updates

Cite this: *Catal. Sci. Technol.*, 2023, **13**, 1059

Gas-phase oxidative dehydrogenation of long chain alkenols for the production of key fragrance ingredients: from Rosalva isomers to Costenal analogues†

Jacopo De Maron, [a] Tommaso Tabanelli, *[a] Francesca Ospitali,[a] Carlos Lopez Cruz,[b] Paolo Righi [a] and Fabrizio Cavani *[a]

Received 22nd October 2022,
Accepted 3rd January 2023

DOI: 10.1039/d2cy01836e

rsc.li/catalysis

The continuous-flow, gas-phase oxidative dehydrogenation (ODH) of an actual mixture of decen-1-ol isomers ("Isorosalva" alcohol) towards the corresponding mixture of aldehydes ("Costenal" analogues, valuable ingredients in perfumes formulation) is herein reported for the first time over noble metal-free catalysts. In particular, the optimisation of the reaction conditions over a copper ferrite (Cu/Fe/O), as well as dedicated characterizations and comparisons between the fresh, the post-reaction (reduced) and regenerated (re-oxidised) catalytic material, allowed us to underline the key role of well dispersed copper oxide over a Fe-enriched spinel in promoting the selective ODH of Isorosalva alcohol. The superior catalytic activity and selectivity of CuO/γ-Fe_2O_3 synthesized *ad hoc* were attributed to the very high dispersion of Cu over the support as well as to a cooperative effect between Cu and Fe species in promoting the redox cycle.

Open Access Article. Published on 04 janvris 2023. Downloaded on 16.07.2024 20:23:18.
This article is licensed under a Creative Commons Attribution-NonCommercial 3.0 Unported Licence.

Introduction

The selective oxidation of complex alcohols (*e.g.*, aromatic, branched or unsaturated fatty alcohols) to the corresponding aldehydes is a fundamental step in the preparation of a wide variety of fragrance ingredients and food additives.[1] Unsaturated fatty aldehydes such as neral, geranial, citronellal and decenal, to cite a few, are among the most important ingredients in perfumery and are used, individually or in combination, in the formulation of most perfume types.[2] Traditionally, the oxidation of fatty alcohols to the corresponding aldehydes has been carried out in high yield using stoichiometric amounts of oxidants such as pyridinium chlorochromate, activated MnO_2, 2-iodobenzoic acid, the Dess–Martin periodinane or the Swern reagent.[3] Unfortunately, all of these methods present safety/toxicity issues, produce large amounts of waste and have significant scale-up issues; on top of that, their sustainability is further reduced because apart from Swern-type oxidations that are carried out in dimethyl sulfoxide, the preferred solvent for all the other methods is dichloromethane.

Owing to these limitations of stoichiometric oxidants, significant efforts have been made in the past years to develop the aerobic oxidation of saturated/unsaturated fatty alcohols in the liquid phase: as a result, several homogeneous catalytic systems based on complexes or salts of Cu,[4–6] Ru,[7–12] Pd,[13–15] Au,[16] Fe[17,18] and Co[19] were reported to be active and selective under mild reaction conditions for the oxidation of model substrates such as 1-octanol, 1-decanol, citronellol and geraniol to the corresponding aldehydes. Still, the scale up of these processes remains difficult due to the cost of noble metals, the difficult catalyst recovery and recycle on an industrial scale, the use of non-green solvents (with the only exception of ref. 9) and the need for organic co-catalysts (*e.g.* DBAB,[4] TEMPO derivatives,[5,6,10,17–19] hydroquinone,[7] and amines[13–15]). These issues prompted the research towards the development of heterogeneous catalysts containing the same active elements immobilized onto a suitable support: the aerobic oxidation of saturated/unsaturated fatty alcohols has been carried out successfully over a number of supported catalysts based on platinum (Pt and Pt/Bi supported onto Al_2O_3 and active carbon),[20] on palladium (Pd supported onto hydrotalcite,[21] mesocellular silica foam (MCF),[22] γ-Al_2O_3 (ref. 23) and MgO (ref. 24)), on ruthenium (Ru supported onto hydroxyapatite[25] and γ-Al_2O_3 (ref. 26 and 27) or immobilized

[a] *Dipartimento di Chimica Industriale "Toso Montanari", Alma Mater Studiorum – Università di Bologna, Viale del Risorgimento 4, 40136 Bologna, Italy.*
E-mail: tommaso.tabanelli@unibo.it
[b] *IFF Benicarló S.L., Avenida Felipe Klein 2, 12580 Benicarló, Spain*

† Electronic supplementary information (ESI) available: Detailed experimental information of catalyst characterisation, namely NH_3 and CO_2-TPD, TPR, XRD, SEM-EDS and TEM analyses. Additional catalytic tests as well as the reactor scheme and blank runs are also reported. See DOI: **https://doi.org/10.1039/d2cy01836e**

Open Access Article. Published on 04 janvris 2023. Downloaded on 16.07.2024 20:23:18.
This article is licensed under a Creative Commons Attribution-NonCommercial 3.0 Unported Licence.

into the pores of MCM-41 (ref. 28)), on silver (Ag supported onto SiO_2 and promoted by physical mixing with CeO_2),[29] on gold (Au supported onto CeO_2,[30] Al_2O_3–CeO_2 mixed oxide[31] and TiO_2 (ref. 32)), and on vanadium (vanadyl acetylacetonate supported on polyaniline).[33] On the other hand, a number of bulk oxides and mixed oxides such as Ru/Co/O,[34] Ru–Co–Al-hydrotalcite,[35] Ru–Co(OH)$_2$–CeO_2,[36] $MnFe_{1.5}Ru_{0.35}Cu_{0.15}O_4$ (ref. 37) and Mn_3O_4 (ref. 38) were reported to be active and selective as well. The oxidation of fatty alcohols in the liquid-phase is usually carried out in batch under mild reaction conditions resulting in good selectivities; moreover, the substrate scope is wide and not limited to vaporizable fatty alcohols. Despite these advantages, the productivity of these liquid-phase oxidations is usually limited by the long reaction times needed and by the need for expensive work up operations.

On the other hand, a gas-phase process can be easily carried out continuously and, with catalyst separation being unnecessary, work up operations are extremely simplified. As an example, light alcohols may be converted into the corresponding aldehydes by means of gas-phase dehydrogenation (DH) with a catalyst such as MgO,[39] mixed oxides of Mg and transition metals possessing redox properties (Fe,[40] Cr[41] or Ga[42,43]), or V-containing oxides[44] such as $FeVO_4$ and V_2O_5, to cite a few. Meanwhile, the literature dealing with the gas-phase DH of fatty alcohols is less investigated and focused on the transformation of model substrates such as octanol[45] and decanol.[46] However, DH processes are endothermic and suffer from several limitations, such as the relatively high reaction temperature required to promote dehydrogenations, the presence of a thermodynamic equilibrium that limits the conversion of the substrate and the occurrence of parasitic reactions such as dehydrations[47] and oligomerisations, the latter often leading to catalyst deactivation due to coke formation. Another drawback of DH processes depends on the reaction mechanism, involving the dissociation of the alcohol into a proton (H^+) and an alkoxide anion (RO^-) on the catalyst surface, followed by a hydride (H^-) transfer from the alkoxide anion to the vicinal proton. In fact, since the hydride can be transferred also to another reactive hydrogen acceptor such as a C=C double bond, DH catalysts foster to a certain extent also the so-called catalytic transfer hydrogenation (CHT).[48,49] For this reason, DH is less suited than ODH for the preparation of unsaturated fatty aldehydes. The oxidative dehydrogenation (ODH) of light alcohols in the gas-phase over a catalyst consisting of bulk or supported Ag,[50] Fe–Mo mixed oxides,[51] $FeVO_4$ and V_2O_5 (ref. 44 and 52) is a well-established technology and represents the prevailing method to produce on a large-scale formaldehyde from methanol[53] and, to a lower degree, acetaldehyde from ethanol.[54] However, the applicability of gas-phase ODH is not limited to light alcohols: in fact, the BASF citral process (which involves the ODH of prenol to prenal over Au, Ag or Cu as a key intermediate step[55]) represents a successful application of ODH to the industrial-scale preparation of a valuable unsaturated fatty aldehyde. The co-feeding of a limited amount of oxygen, with respect to DH processes, allows the reaction temperature to be lowered by promoting the oxidation of the co-produced hydrogen to water *via* a concerted mechanism, eventually shifting the thermodynamic equilibrium towards the product side. However, despite the potential of gas-phase ODH, this reaction remains very challenging, because of the high reactivity of fatty alcohols and aldehydes at the relatively high temperatures required by their vaporization and reaction. As a consequence, the academic literature available on this topic is narrower than that about liquid-phase oxidations, and deals mostly exclusively with octanol (as a model substrate) and catalytic systems based on either gold (Au/SiO_2,[56] Au–Ni alloy/SiO_2,[57] Au/Cu-fibres[58,59] and Au/Ni fibres[60]) or silver (bulk Ag,[61] Ag supported over a zeolite coated Cu grid,[62] Ag/silicon nanowire arrays[63] and Ag-Cu/SiC[64]).

Among fatty aldehydes, the isomers of decenal are notable ingredients in the formulation of perfumes and other personal care products, not only as single isomers (*i.e.*, dec-9-enal, commercial name "Costenal")[65] but also as a combination of isomers: as an example, mixtures of dec-6-enal, dec-7-enal and dec-8-enal with well-defined compositions were patented as novel ingredients by International Flavors & Fragrances Inc.[66] Despite their relevance, very few catalytic processes have been proposed as alternatives to the traditional oxidation of dec-9-en-1-ol (commercially known as "Rosalva") with stoichiometric reactants such as pyridinium chlorochromate,[67] Dess–Martin periodinanes,[68] activated MnO_2,[69] $K_2S_2O_8$/$NiSO_4$ in the presence of a base[70] or oxalyl dichloride, DMSO and alkyl amines in Swern-type oxidations),[71] which are not sustainable for large-scale production. To the best of our knowledge, the liquid-phase aerobic oxidation of pure Rosalva to Costenal has been reported only twice: with air and a homogeneous tetrapropylammonium perruthenate catalyst,[12] and with pure O_2 and a heterogeneous Ru–Co oxide catalyst.[34]

Similarly, also the gas-phase ODH of Rosalva to Costenal was reported only twice, by Gallezot *et al.*[65] over a 4.5% Ag/SiC catalyst charged into a traditional fixed bed reactor and by Cao *et al.*[72] with an Ag/SiO_2 catalyst deposited onto a continuous-flow microreactor. Considering that a pure Rosalva alcohol can be easily isomerised into a selected mixture of its isomers,[66] in this study an actual mixture of decen-1-ols ("Isorosalva" alcohols), produced and supplied by International Flavors & Fragrances Inc., was used as the starting material for the continuous-flow, gas-phase ODH aimed at the production of the corresponding mixture of aldehydes ("Opalene" aldehydes), directly exploitable in fragrance formulation. Moreover, herein we report for the first time this peculiar ODH reaction promoted by a cheap, noble metal-free, non-stoichiometric Cu-ferrite catalyst with a Fe-to-Cu ratio equal to 4 ($Cu_{0.6}Fe_{2.4}O_{4.2}$) and by a supported copper oxide catalyst (6 wt% CuO/γ-Fe_2O_3). The comparison between our synthetic strategy and the alternatives reported in the literature is depicted in Scheme 1. In particular, dedicated catalytic tests showed that our catalyst performs

 This journal is © The Royal Society of Chemistry 2023

Open Access Article. Published on 04 janvris 2023. Downloaded on 16.07.2024 20:23:18.
This article is licensed under a Creative Commons Attribution-NonCommercial 3.0 Unported Licence.

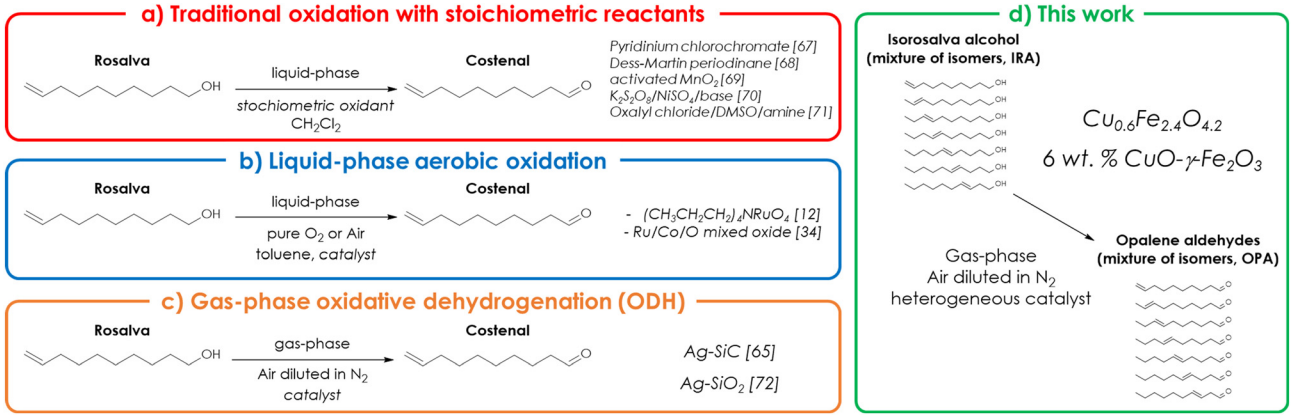

Scheme 1 Comparison between a) oxidation of Rosalva to Costenal with traditional stoichiometric oxidants, b) aerobic oxidation of Rosalva with air/O_2 in the liquid-phase, c) oxidative dehydrogenation (ODH) of Rosalva in the gas-phase and d) oxidative dehydrogenation (ODH) of an Isorosalva mixture of isomers in the gas-phase.

better, in terms of selectivity, than a typical V_2O_5–TiO_2 benchmark catalyst for the ODH of light alcohols; moreover, analyses of the product distribution and an in-depth characterisation of the catalytic materials allowed us to highlight that the co-presence of both Cu and Fe result in a synergistic effect that boosts the selectivity to the desired Opalene mixture.

Experimental

Catalyst preparation

A copper ferrite with a nominal Fe/Cu atomic ratio of 4 (henceforth in the text, Cu/Fe/O) was synthesized adapting a co-precipitation technique from the literature.[73] Briefly, 200 mL of a solution containing 0.5 mol L^{-1} $Fe(NO_3)_3{\cdot}9\ H_2O$ (Sigma-Aldrich, 98%), and 0.125 mol L^{-1} $Cu(NO_3)_2{\cdot}2.5\ H_2O$ (Sigma-Aldrich, 98%) was slowly added dropwise under vigorous stirring to 300 mL of a solution containing 2 mol L^{-1} NaOH (Sigma-Aldrich, 98%). At the end of the addition, the resulting brown suspension was aged for 1 h under stirring, filtered over a Buchner funnel, and washed with deionized water until pH 7 to remove hydroxide, nitrate, and sodium ions. The resulting wet solid was dried overnight at 120 °C, ground in an agate mortar, and calcined with a heating rate of 5 °C min^{-1} up to 450 °C; the final temperature was kept for 4 h. The vanadium oxide supported over titania (V_2O_5/TiO_2) was prepared by means of wet impregnation, adapting the procedure reported here.[74] To obtain a wt% of V equal to 3.6, equivalent to a 6 wt% of V_2O_5, 9.4 g of commercial TiO_2 (9.4 g, CristalACTiV DT-51) was suspended under stirring in 30 mL of a hot (≈50 °C) solution containing 0.22 mol L^{-1} NH_4VO_3 (Sigma Aldrich, 99%). The suspension was stirred for 1 h, evaporated in a rotavapor and finally dried in an oven at 120 °C overnight. The resulting material was ground in an agate mortar and calcined with a heating rate of 5 °C min^{-1} up to 500 °C; the final temperature was kept for 5 h. γ-Fe_2O_3 (maghemite) was prepared from commercial Fe_3O_4 (magnetite, Sigma-Aldrich, 97%, particle size 50–100 nm) by calcination at 200 °C for 3 h. Upon heating the powder changed its colour from black to brown-reddish and maintained its magnetic properties. The copper oxide supported over silica (CuO/SiO_2) was prepared by means of incipient wetness impregnation. To obtain a wt% of Cu(0) equal to 5, equivalent to 6.1 wt% of CuO, 1.83 g of $Cu(NO_3)_2{\cdot}2.5\ H_2O$ (Sigma-Aldrich, 98%) was dissolved in 20 mL of deionized water and added dropwise to 9.5 g of SiO_2 (Grace 360) until the mud point was reached (2 mL of solution per gram of support). The resulting wet powder was dried in an oven at 120 °C for 2 h and calcined with a heating rate of 5 °C min^{-1} up to 450 °C; the final temperature was kept for 4 h. The copper oxide supported over maghemite ($CuO/\gamma\text{-}Fe_2O_3$) was prepared by means of incipient wetness impregnation in the same way as CuO/SiO_2. In order to obtain a wt% of Cu(0) equal to 5, equivalent to 6.1 wt% of CuO, 1.83 g of $Cu(NO_3)_2{\cdot}2.5\ H_2O$ was dissolved in 5.5 mL of deionized water and added dropwise to 9.5 g of Fe_3O_4 (magnetite, Sigma-Aldrich, 97%, particle size 50–100 nm) until the mud point was reached (0.55 mL of solution per gram of support). The resulting wet powder was dried in an oven at 120 °C for 2 h and calcined with a heating rate of 5 °C min^{-1} up to 450 °C; the final temperature was kept for 4 h. All the catalysts were charged into the reactor in the form of pellets with a granulometry between 30 and 60 mesh, which were obtained by grinding a self-sustaining disk (height ≈ 1 mm, diameter ≈ 30 mm) through a 30-mesh sieve placed on top of a 60-mesh sieve and collecting the fraction of pellets trapped between the two sieves.

Catalyst characterization

The XRD powder patterns of all the catalysts were collected using a Bragg–Brentano Philips X'Pert diffractometer and Cu Kα radiation (λ = 1.54178 Å, Ni-filtered). The average size of the coherently scattering domain (CSD) of materials was calculated applying the Scherrer equation (eqn (1)):

Open Access Article. Published on 04 janvris 2023. Downloaded on 16.07.2024 20:23:18.
This article is licensed under a Creative Commons Attribution-NonCommercial 3.0 Unported Licence.

$$\mathrm{CSD} = (K\cdot\lambda)/(\beta\cdot\cos\vartheta) \quad (1)$$

where the shape factor is K = 0.9, the instrumental line broadening is β^{INST} = 0.07°, and β = (FWHM − β^{INST}). The specific surface area of the catalyst was measured by the single-point BET technique at −196 °C (77 K) using a Fisons Sorpty 1750 instrument; in some cases, N_2 multipoint adsorption–desorption isotherms were also collected using a Micromeritics ASAP 2020 instrument. The acidity and basicity of the catalysts were measured by means of temperature-programmed desorption (TPD) of NH_3 and CO_2 from 0.2 g of sample, using a Micromeritics AutoChem II 2920 instrument equipped with a TCD. The H_2 uptake of the catalysts was measured by means of temperature-programmed reduction (TPR). A detailed description of TPD and TPR experiments can be found in the ESI† (Chapter S1). Energy dispersive spectrometry (EDS) analysis was carried out with a Zeiss EP EVO 50 scanning electron microscope (SEM) equipped with an INCA X-Act penta FET Precision detector (Oxford Instruments Analytical) for the elemental mapping of elements. Spectra were recorded for 60 seconds with an accelerating voltage of 20 kV. High resolution transmission electron microscopy (HRTEM) images were collected using an FEI TECNAI F20 TEM microscope operating at 200 KeV and equipped with an EDS probe for elemental microanalysis and a scanning TEM accessory. TEM images were taken in phase-contrast mode; STEM images were recorded using a high angle annular dark field detector (HAADF). Before analysis, each sample was suspended in ethanol and subjected to ultrasound for 20 minutes; then, a drop of the suspension was deposited on a Quantifoil carbon film supported by a gold grid and then dried at 100 °C. Raman spectra were collected using a Renishaw InVia Raman spectrometer configured with a Leica DM LM microscope; the exciting sources were an Ar^+ laser (514.5 nm) and a diode laser (785.0 nm), and the spectral range was 100–2000 cm^{-1}.

Catalytic tests

All catalytic tests were carried out at atmospheric pressure on the gas-phase plant shown in Fig. S1 (ESI†). The reactor was a conventional fixed bed down-flow quartz reactor, and all the catalysts were charged as pellets with size between 30 and 60 mesh.

The liquid reactant "Isorosalva Alcohol" (IRA, mixture of isomers of decen-1-ol provided by Iff) was injected with a KD Scientific Legacy 100 volumetric pump into a thin stainless-steel line (1/16 inches of diameter) and directly driven ≈5 cm above the catalytic bed with 10 mL min^{-1} N_2. A second flux of pre-heated (250 °C) air diluted with N_2 was driven to the top of the reactor to obtain the desired molar fraction of O_2 and the desired total flux. Usually, the catalyst was flowed with the same air/N_2 mixture to be used during the catalytic test and heated up to reaction temperature at 20 °C min^{-1}; the final temperature was kept for 30 min before starting to feed the liquid reactant. The effluent from the reactor was bubbled through two cold traps in series: the former was filled with 15 mL of acetonitrile (AcCN, Sigma-Aldrich, 99.8%) and kept at room temperature to absorb the condensable products; the latter was filled with glass spheres and kept at 0 °C by means of an ice bath to condensate the AcCN stripped from the first trap. At regular intervals of time, the reaction mixture was transferred from the first cold trap to a 50 mL flask, together with the AcCN needed to wash the lower portion of the reactor below the catalytic bed and to rinse the cold trap 3 times. Finally, 1 g of dodecane (Sigma-Aldrich, 99%) solution (4×10^{-5} mol g^{-1}) was added as the internal standard. All catalytic tests were carried out for the time required to obtain at least 5 samples (5–6 h) to be analysed by means of GC-FID; the mean values of conversion and selectivities were calculated once steady-state conditions were achieved, usually during the last 3 h of time on stream. The gas mixture exiting the cold traps were driven to an Agilent 8860 GC instrument equipped with an FID and TCD. The quantification of the condensable products was carried out offline with an Agilent HP-5 capillary column (30 m × 0.32 mm × 0.25 μm) connected to the FID. The quantification of the gaseous products (O_2, N_2, CO, CO_2) was carried out online with a set of two parallel columns combining an Agilent CP-Molsieve 5 Å capillary column and an Agilent CP-PoraBOND Q capillary column ("Agilent J&W Select Permanent Gases/CO_2") connected to the TCD. An Agilent Technologies 6890 gas chromatograph equipped with an Agilent HP-5 capillary column (30 m × 250 μm × 1.05 μm) and coupled to an Agilent Technologies 5973 mass analyser (GC-MS) was used to identify unknown products; also, the retention times of unknown products were compared to those of purchased standard reference compounds. The following equations were used to calculate Isorosalva Alcohol conversion (X IRA, eqn (2)), yields (Y_i, eqn (3)), selectivities (S_i, eqn (4)), sum of yields (Yield Sum, eqn (5)), and carbon balance (C-balance, eqn (6)). All these parameters were calculated in terms of moles of carbon.

$$X\ \mathrm{IRA} = (\mathrm{mol}^{\mathrm{IRA}}_{\mathrm{CIN}} - \mathrm{mol}^{\mathrm{IRA}}_{\mathrm{COUT}}/\mathrm{mol}^{\mathrm{IRA}}_{\mathrm{CIN}}) \times 100 \quad (2)$$

$$Y_i = (\mathrm{mol}^{i}_{\mathrm{COUT}}/\mathrm{mol}^{\mathrm{IRA}}_{\mathrm{CIN}}) \times 100 \quad (3)$$

$$S_i = (Y_i)/(X\ \mathrm{IRA}) \times 100 \quad (4)$$

$$\mathrm{Yield\ Sum} = \sum_i Y_i \quad (5)$$

$$\text{C-balance} = (\text{Yield Sum})/(X\ \mathrm{IRA}) \times 100 \quad (6)$$

Results and discussion

Characterization of fresh catalysts

The main physico-chemical features of the catalysts are listed in Table 1. CuO/SiO_2 possessed the highest specific surface area (455 m^2 g^{-1}) among the materials investigated, followed by the Cu/Fe/O mixed oxide (165 m^2 g^{-1}), V_2O_5/TiO_2 (22 m^2 g^{-1}), $CuO/\gamma\text{-}Fe_2O_3$ (9 m^2 g^{-1}) and $\gamma\text{-}Fe_2O_3$ (9 m^2 g^{-1}). Apart

 This journal is © The Royal Society of Chemistry 2023

Open Access Article. Published on 04 janvris 2023. Downloaded on 16.07.2024 20:23:18.
This article is licensed under a Creative Commons Attribution-NonCommercial 3.0 Unported Licence.

Table 1 Physico-chemical properties and elemental composition of fresh catalysts

	SSA[a] [$m^2\ g^{-1}$]	CSD size[b] [nm]	Element or oxide content[c,d] [wt%]
V_2O_5/TiO_2	22	125 (V_2O_5) 58 (TiO_2)	V_2O_5 = 6.2 (6)
Cu/Fe/O	165	5 (Cu-ferrite)	Cu = 14.3 (16) Fe = 57.4 (56)
CuO/SiO_2	455	35 (CuO)	CuO = 6.9 (6.1)
CuO/γ-Fe_2O_3	9	81 (γ-Fe_2O_3)	CuO = 4.8 (6.1)
γ-Fe_2O_3	9	78 (γ-Fe_2O_3)	—

[a] SSA measured by single-point BET. [b] CSD size calculated from XRD. [c] Elemental analysis carried out by SEM-EDS. [d] Theoretical values are reported within brackets.

from the precipitated copper ferrite, for all the other materials the final specific surface area was mainly affected by the initial surface area of the oxide support.

The XRD powder pattern of Cu/Fe/O (Fig. S2a†) was characterized by broad reflections, attributable to a nano-crystalline, defective spinel structure (CSD size = 5 nm, Table 1), with no substantial impurities of segregated CuO_x or FeO_x. The high defectivity of Cu/Fe/O ($Cu_{0.6}Fe_{2.4}O_{4.2}$) was attributed to the excess of the trivalent cation Fe(III) with respect to the divalent cation Cu(II) deviating from that of the stoichiometric spinel $CuFe_2O_4$. As a result, the material displayed a relatively high specific surface area and a small CSD size. The diffractogram of V_2O_5/TiO_2 (Fig. S2b†), in agreement with the literature,[75] arose from the superimposition of the pattern of TiO_2 anatase and V_2O_5, with the former being largely predominant; both phases had high crystallinity. The XRD powder pattern of CuO/SiO_2 (Fig. S3a†) was characterized by a very broad band, centred at 2θ = 22° and attributable to amorphous silica, plus a set of sharper reflections that were ascribed to well-developed CuO tenorite crystals (CSD size = 35 nm, Table 1). The pattern of γ-Fe_2O_3 (Fig. S3b†) was characterized by sharp reflections, attributable to the pattern of the maghemite cubic spinel (CSD size = 78 nm, Table 1). The maghemite pattern was distinguished from that of the parent magnetite (Fe_3O_4 spinel) because all the reflections of the γ-form were shifted towards higher 2θ values, corresponding to lower *d*-spacings.[76] Finally, the XRD powder pattern of CuO/γ-Fe_2O_3 is shown in Fig. S4:† unlike CuO/SiO_2, in this case a well-defined pattern attributable to CuO was absent: this can mean either that the dispersion of copper was much higher on maghemite than on silica, or that upon calcination Cu(II) was incorporated into the newly formed γ-Fe_2O_3 structure resulting in a Cu enriched maghemite. Instead, the diffractogram displayed a well-defined pattern of maghemite (CSD size = 81 nm, Table 1), plus a few weak but sharp reflexes attributable to an impurity of hematite (α-Fe_2O_3, CSD size = 42 nm, Table 1).

The elemental composition of the catalysts was verified by means of SEM-EDS. The experimental wt% of V_2O_5 on TiO_2 measured by EDS was 6.2%, in good agreement with the theoretical value of 6. In the case of Cu/Fe/O, the EDS elemental map of Cu (Fig. S5b†) indicates that it was homogeneously distributed in the sample, which was a true mixed metal solid solution. The electron images and elemental maps of CuO/SiO_2, as well as its Raman spectrum (both shown in Fig. S6†) indicated that Cu was concentrated in specific areas, forming flower-like crystals of tenorite (CuO)[77] with ≈100 nm diameter. Conversely, the elemental maps of CuO/γ-Fe_2O_3 suggested that Cu was more homogeneously distributed in the sample (Fig. S7b†).

The high-resolution TEM characterization of Cu/Fe/O is shown in Fig. S8:† the material was formed by small, quasi-spherical and poorly crystalline grains with an average diameter of 5 nm, in agreement with the CSD size calculated from the XRD diffractogram with the Scherrer equation (eqn (1)). On the other hand, the TEM electron images reported in Fig. S9† showed that CuO/γ-Fe_2O_3 was made of much bigger grains (100–150 nm) and that supported CuO nanoparticles were not systematically present over the support. Nonetheless, the EDS microanalysis carried out over more than 10 grains showed that Cu was always present. In particular, the mass fraction of CuO ranged from 3.7 to 7.1 wt%, with an average value of 5.3 wt%, in good agreement with the value of 4.8 wt% obtained with the SEM elemental analysis, suggesting that Cu-species were extremely dispersed over the support, possibly forming small clusters, overlayers or being partially incorporated into the defects of γ-Fe_2O_3.

ODH of Isorosalva alcohol over Cu/Fe/O and V_2O_5/TiO_2

A series of preliminary blank runs was carried out in order to optimize the reaction conditions and the feeding system setup. The results of two blank runs carried out at 350 °C reaction temperature, contact time (τ) of 1 s and with a feed mixture containing 5 mol% of Isorosalva Alcohol (IRA), 5 mol% of O_2, and 90% of N_2 are shown in the ESI† (Fig. S10). Unknown compounds obtained during the catalytic tests were grouped together and are reported in figures under the category "Others". When IRA was vaporized by injecting the suitable liquid flow rate in a 1/8″ stainless-steel line heated at 250 °C before the reactor (blank run 1, Fig. S10†), a significant fraction of the reactant decomposed (X IRA = 25%) and the carbon balance was very low (<50%). On the other hand, when IRA was fed directly into the reactor at about 5 cm above the catalytic bed by means of a stainless-

Open Access Article. Published on 04 janvris 2023. Downloaded on 16.07.2024 20:23:18.
This article is licensed under a Creative Commons Attribution-NonCommercial 3.0 Unported Licence.

steel capillary line, IRA conversion was 7% and the carbon balance became higher than 90% (blank run 2, Fig. S10†). These results indicate that IRA underwent some uncatalyzed homogeneous reactions in the gas-phase when exposed to high temperatures for a relatively long time, as it was in the case of blank run 1; these reactions induced the extensive fouling of the reactor inner walls, both before and after the catalytic bed, as shown in Fig. S11.† However, the extent of these unwanted homogenous reactions can be reduced either by reducing the dead volume of the reactor, or by reducing the time spent by IRA inside the reactor at high temperature. This way, the extent of the fouling was effectively reduced and limited to the reactor walls below the catalytic bed in blank run 2, as shown in Fig. S11.† Therefore, all the following catalytic tests were carried out with the same IRA feeding system used in blank run 2.

Initially, the ODH of IRA was carried out over Cu/Fe/O, V_2O_5/TiO_2 and without a catalyst (for comparison) at 300 °C temperature, τ = 1 s and with a feed mixture IRA/O_2/N_2 = 5/5/90; under these conditions, the O_2 in the feed was two-fold the amount required by the stoichiometry of the desired reaction. The results of these catalytic tests are reported as a bar chart in Fig. 1 in terms of conversion of IRA (*X* IRA), selectivities to products (*S*), and carbon balance (C-balance); these parameters were calculated in terms of moles of carbon. The conversion of IRA at 300 °C was negligible without a catalyst, therefore the occurrence of homogeneous reactions under these conditions can be ruled out. As expected, V_2O_5/TiO_2 was relatively active in the ODH of IRA: the conversion under these conditions was 34% and O_2 was consumed entirely. OPA was the main product in the reaction mixture with a selectivity of 32%, followed by several isomers of decadiene (*S* DD = 20%) and carbon oxides (*S* CO_x = 18%, with CO_2 being largely predominant with respect to CO). Decadienes are likely to be formed by the dehydration of IRA over acidic sites,[78] as shown in Scheme 2 (reaction b), while carbon oxides are formed by the complete combustion of the reactant or products. Apart from CO and CO_2, all the products found in the reaction mixture contained 10 C atoms; therefore, the occurrence of the oxidative cleavage of C=C double bonds[79] was ruled out. When IRA was fed over Cu/Fe/O, its conversion (23%) was lower than the one obtained over V_2O_5/TiO_2 under the same conditions, but the two materials displayed a similar activity for the ODH, because the OPA yields with V_2O_5/TiO_2 and Cu/Fe/O were 11% and 12%, respectively. The superior selectivity of Cu/Fe/O to the desired products (*S* OPA = 51%) arose from its negligible activity for the unwanted dehydration of IRA to DD. Similarly, with Cu/Fe/O also the selectivity to CO_x was higher than that obtained with V_2O_5/TiO_2.

To better understand the structure–activity relationship governing the reaction scheme, the two catalysts were further characterized by means of NH_3- and CO_2-TPD to compare their acid–base surface features, and by means of TPR with H_2 to compare their reducibility. The NH_3- and CO_2-TPD profiles for Cu/Fe/O are shown in Fig. S12a and b† respectively, while those for V_2O_5/TiO_2 are reported in Fig. S13a and b† respectively. Also, the density of weak, medium-strength and strong acidic and basic sites measured by deconvolution of the experimental desorption profiles is reported in Table 2 for both materials. Cu/Fe/O was amphoteric and possessed a higher overall density of acidic sites (0.98 μmol m^{-2} of NH_3) than basic sites (0.66 μmol m^{-2} of CO_2). However, the acidic sites of Cu/Fe/O were of medium-strength (two desorption events centred at 223 and 303 °C), while the distribution of basic sites was more complex and several types of sites were shown (four desorption events centred at 117, 242, 310 and 440 °C).

V_2O_5/TiO_2 was amphoteric as well, but it possessed an overall density of both acidic and basic sites higher compared to Cu/Fe/O (3.6 μmol m^{-2} of NH_3 and 3.0 μmol m^{-2} of CO_2). In conclusion, the stronger acidity, in terms of both density and desorption temperature, of V_2O_5/TiO_2 is likely to be responsible for the unwanted dehydration of IRA to DD. The redox properties of Cu/Fe/O and V_2O_5/TiO_2 were characterized by means of TPR with H_2 and their reduction profiles as well as a detailed discussion can be found in Chapter S2 and Fig. S14 in the ESI.† The ODH of IRA was further investigated using the Cu/Fe/O catalyst with the aim to increase the yield of OPA. Two catalytic tests were carried out by increasing either the reaction

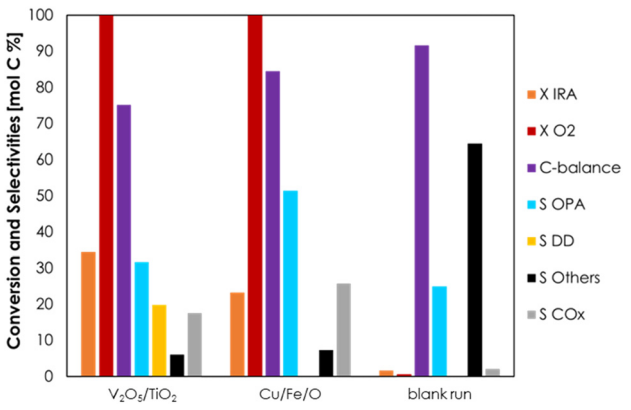

Fig. 1 ODH of IRA over V_2O_5/TiO_2, Cu/Fe/O and without any catalyst. Reaction conditions: volume of catalyst = 1 cm^3, temperature = 300 °C, IRA/O_2/N_2 = 5/5/90 mol%, contact time (τ) = 1 second. Symbols: Isorosalva Alcohol conversion (*X* IRA, orange), oxygen conversion (*X* O_2, dark red), carbon balance (C-balance, purple), opalene selectivity (*S* OPA, light blue), decadiene selectivity (*S* DD, yellow), other by-products' selectivity (*S* Others, black) and CO_x selectivity (*S* CO_x, grey). Mean values calculated at the steady-state during the last 3 h of time on stream.

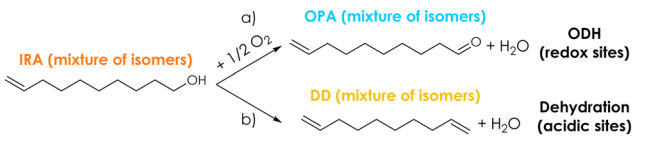

Scheme 2 Proposed reaction pathways for a) the desired ODH of IRA towards OPA and b) the parallel parasitic dehydration of IRA towards a mixture of decadiene (DD) isomers.

This journal is © The Royal Society of Chemistry 2023

Open Access Article. Published on 04 janvris 2023. Downloaded on 16.07.2024 20:23:18.
This article is licensed under a Creative Commons Attribution-NonCommercial 3.0 Unported Licence.

Table 2 Distribution of weak, medium-strength and strong acidic and basic sites on V_2O_5/TiO_2 and Cu/Fe/O measured by means of ammonia and carbon dioxide temperature programmed desorption

	Acidity [μmol m^{-2} of desorbed NH_3]				Basicity [μmol m^{-2} of desorbed CO_2]			
	Weak[a]	Medium[b]	Strong[c]	Total	Weak[a]	Medium[b]	Strong[c]	Total
V_2O_5/TiO_2	0	3.6	0	3.6	0.13	3.0	0	3.13
Cu/Fe/O	0	0.98	0	0.98	0.29	0.17	0.2	0.66

[a] Desorption below 200 °C. [b] Desorption between 200 and 350 °C. [c] Desorption above 350 °C.

temperature, from 300 to 350 °C (Fig. 2a), or the contact time from 1 to 4.5 s (Fig. 2c) and the results were compared to those of the catalytic tests carried out at 300 °C and τ = 1 s (Fig. 2b). The increase of temperature from 300 °C to 350 °C, while maintaining a contact time of 1 s (Fig. 2a), led to only a moderate increase of IRA conversion (from 23% to 32%). At the same time, OPA selectivity shrank from 51% to 22% because it was consumed by consecutive reactions, such as the formation of 10-nonadecadienones (NDD, red bars, *S* = 13%) and other unknown by-products (black bars, *S* = 16%). Also, the carbon balance decreased from 85% at 300 °C down to 70% at 350 °C, suggesting the occurrence of other unwanted reactions (*e.g.*, homogeneous reactions, coking and fouling). The increase of the contact time from 1 s to 4.5 s at 300 °C (Fig. 2c) led to a more significant increment of IRA conversion (from 23% to 52%) but also in this case OPA underwent consecutive reactions that decreased its selectivity from 51% down to 35% and led to the formation of decenoic acids (DA, green bars *S* = 8%) and 10-dodecatrienals (ODT, blue bars, *S* = 19%). Remarkably, increasing the contact time did not negatively affect the carbon balance, suggesting that some unwanted reactions (*e.g.*, gas-phase homogeneous reactions, coking and fouling) were fostered mainly by high temperatures, in agreement with the results of the blank runs at 350 °C (Fig. S10 and S11†). Summarising this new information, a more detailed reaction scheme is shown in Scheme 3. The presence of DA among the reaction products was explained by the consecutive oxidation of OPA (Scheme 3, reaction c), which was fostered by harsher reaction conditions. Then, the resulting DA underwent a ketonization reaction[80] forming the symmetric C_{19} ketone NDD (Scheme 3, reaction e); in agreement with previous results[43,80] the ketonization was particularly favoured at 350 °C and DA were quantitatively transformed into NDD. Finally, the C_{20} aldehyde ODT was formed by the aldol condensation of OPA with itself (Scheme 3, reaction d), which was fostered by an increase of the contact time (*e.g.*, 4.5 seconds). Considering the stoichiometry of the selective ODH of IRA to OPA (Scheme 3, reaction a), the O_2 fed into the system was always two-fold the one required for the complete conversion of IRA. However, O_2 was always quantitatively consumed under all conditions reported in Fig. 2, because it was unselectively converted to overoxidation products (*i.e.*, CO_2). Results reported in Fig. 2 showed that an increase of the contact time was the most effective way to improve IRA conversion without fostering its overoxidation to CO_x. Therefore, we decided to investigate in more depth the behaviour of the Cu/Fe/O catalyst under these conditions (*e.g.*, 300 °C of temperature, τ = 1 s, feed mixture $IRA/O_2/N_2$ = 5/5/90 mol%) as a function of time on stream; the results are shown in Fig. 3. During the first hour of reaction, the Cu-ferrite was extremely active, and the conversion of IRA was complete, but the C-balance was lower than 20% and CO_x were almost the sole products of the reaction. Then, starting from the second hour on stream, the selectivity to condensable products and the C-balance increased, and stabilized after 3 h on stream. At the same time, the conversion of IRA decreased steadily down to half of its initial value during 5 h on stream.

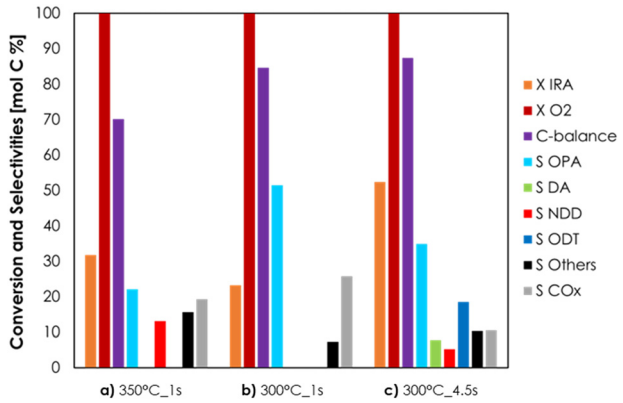

Fig. 2 ODH of IRA over Cu/Fe/O as a function of reaction temperature and contact time. Reaction conditions: volume of catalyst = 1 cm^3 (τ = 1 second) or 3 cm^3 (τ = 4.5 second), $IRA/O_2/N_2$ = 5/5/90 mol%. Symbols: Isorosalva Alcohol conversion (*X* IRA, orange), oxygen conversion (*X* O_2, dark red) carbon balance (C-balance, purple), opalene selectivity (*S* OPA, light blue), decenoic acid selectivity (*S* DA, green), 10-nonadecadienone selectivity (*S* NDD, red), 2-octyldodecatrienal selectivity (*S* ODT, blue), other by-products' selectivity (*S* Others, black) and CO_x selectivity (*S* CO_x, grey). Mean values calculated at the steady-state during the last 3 h of time on stream.

Therefore, we decided to stop the feeding of IRA and regenerate the catalyst *in situ* by feeding 50 mL min^{-1} of air diluted with 10 mL min^{-1} N_2 at 400 °C for 3 h. Then, the feeding of IRA was resumed and, surprisingly, a completely different product distribution was obtained: in fact, OPA became the main product of the reaction over the regenerated Cu/Fe/O (*S* OPA = 70%, *X* IRA = 45%, values calculated as the average value between the 7th and the 16th hour on stream). At the same time, the obtained C-balance was excellent, and the selectivity to the consecutive products NDD and ODT, which were produced in significant amounts over the fresh Cu/Fe/O, dropped from 18 down to 3% and

Open Access Article. Published on 04 janvris 2023. Downloaded on 16.07.2024 20:23:18.
This article is licensed under a Creative Commons Attribution-NonCommercial 3.0 Unported Licence.

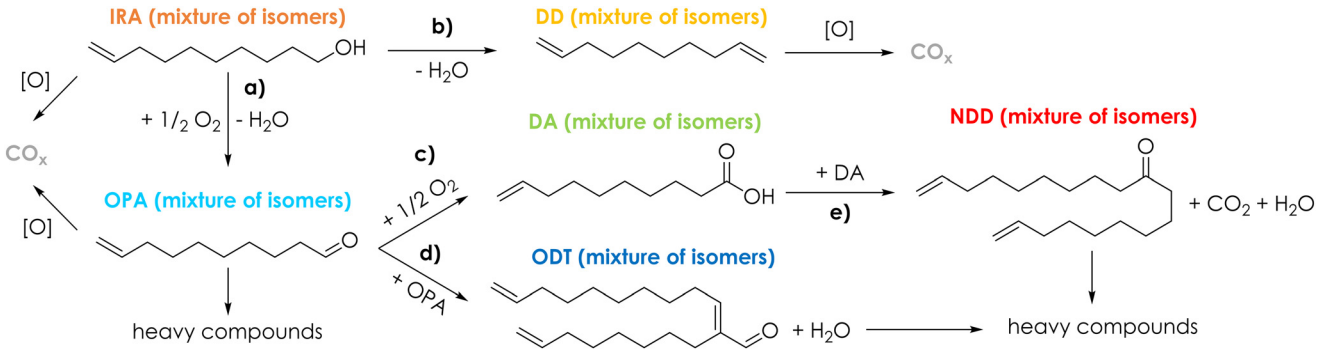

Scheme 3 Proposed complete reaction scheme: a) ODH of IRA towards OPA; b) parallel parasitic dehydration of IRA towards DD; c) overoxidation of OPA towards DA; d) aldol condensation of OPA to ODT; e) ketonization of DA to NDD; other reactions include the formation of heavy compounds on the catalyst surface and the total oxidation to CO_x.

from 5 to 0%, respectively. Finally, the regenerated Cu/Fe/O catalyst maintained a stable catalytic performance for 10 h. Interestingly, during the very first hour of reaction CO_2 was the major product over both the fresh and the freshly regenerated Cu/Fe/O catalyst. The outcome of the catalytic test reported in Fig. 3 indicated that the regeneration *in situ* after the first run played a key role in improving the catalyst selectivity to OPA.

Characterization of Cu/Fe/O after reaction and after regeneration

The redox mechanism of ODH postulates that, as a consequence of the reduction of a metal cation (*e.g.*, Cu^{2+} or Fe^{3+} in the case of Cu/Fe/O) by the organic reactant, the formation of the co-produced water occurs at the expense of the lattice oxygen of the metal oxide. Then, the catalytic cycle is closed by the reoxidation of the reduced metal by the molecular O_2 in the gaseous feed. Considering that under all the reaction conditions investigated so far, the conversion of O_2 was quantitative, it is likely that the reoxidation of the catalyst was limited by the complete consumption of O_2 in the feed, resulting in a catalyst that under reaction conditions was presumably strongly reduced. Upon the ODH of IRA followed by *in situ* regeneration, the fresh Cu/Fe/O underwent a transformation that significatively enhanced its selectivity to the desired product OPA. Therefore, a small portion of the catalyst employed in the experiment shown in Fig. 3 was withdrawn from the reactor before and after the *in situ* regeneration; then, these materials were thoroughly characterized. Samples were labelled as follows: Cu/Fe/O-F (fresh), Cu/Fe/O-AR (after reaction) and Cu/Fe/O-R (regenerated).

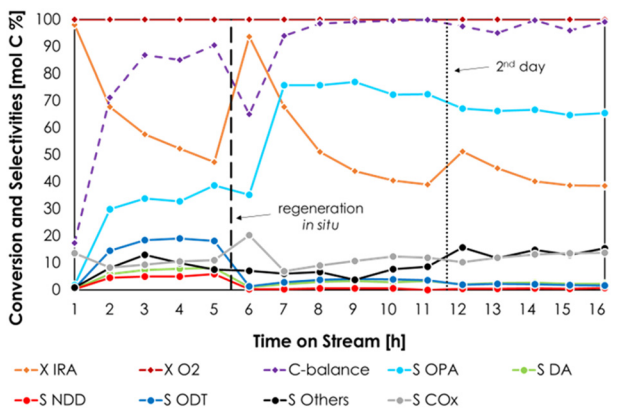

Fig. 3 ODH of IRA over Cu/Fe/O as a function of the time on stream. Reaction conditions: volume of catalyst = 1 cm^3, temperature = 300 °C, IRA/O_2/N_2 = 5/5/90 mol%, contact time (τ) = 4.5 seconds. Symbols: Isorosalva Alcohol conversion (X IRA, orange), oxygen conversion (*X* O_2, dark red) carbon balance (C-balance, purple), opalene selectivity (*S* OPA, light blue), decenoic acid selectivity (*S* DA, yellow), 10-nonadecadienone selectivity (*S* NDD, red), 2-octyldodecatrienal selectivity (*S* ODT, blue), other by-products' selectivity (*S* Others, black) and CO_x selectivity (*S* CO_x, grey).

The XRD powder patterns of Cu/Fe/O-F, Cu/Fe/O-AR and Cu/Fe/O-R are shown in Fig. 4a and b. The diffractogram of Cu/Fe/O-AR (Fig. 4a, red) was characterized by the pattern of a spinel phase as it was for Cu/Fe/O-F, plus three peaks attributable to metallic Cu centred at 43, 50 and 74 2θ degrees. Therefore, Cu/Fe/O was reduced during the ODH of IRA leading to the segregation of metallic Cu over a Fe-enriched spinel. The formation of the latter was confirmed by the small shift towards lower 2θ angles of the reflections of the spinel phase (Fig. 4b). Moreover, the reflections attributable to the Fe-enriched spinel-phase were sharper than the ones of Cu/Fe/O-F, indicating that the crystallinity of the catalysts increased during the ODH of IRA; hence, the CSD size of the spinel calculated by the Scherrer equation (eqn (1)) increased from 5 nm to 10 nm and the SSA dropped from 165 $m^2\ g^{-1}$ to 63 $m^2\ g^{-1}$. In the diffractogram of Cu/Fe/O-R (Fig. 4a, light blue) the reflections of metallic Cu disappeared leaving only a spinel phase, plus a few small reflections attributable to hematite (α-Fe_2O_3); no reflections attributable to CuO or Cu_2O were found. The XRD characterization suggested that upon regeneration all metallic Cu was oxidised to Cu(II) and re-incorporated into the spinel structure of the catalyst, as demonstrated by the shift of the reflections of the spinel phase of Cu/Fe/O-R with

 This journal is © The Royal Society of Chemistry 2023

Open Access Article. Published on 04 janvris 2023. Downloaded on 16.07.2024 20:23:18.
This article is licensed under a Creative Commons Attribution-NonCommercial 3.0 Unported Licence.

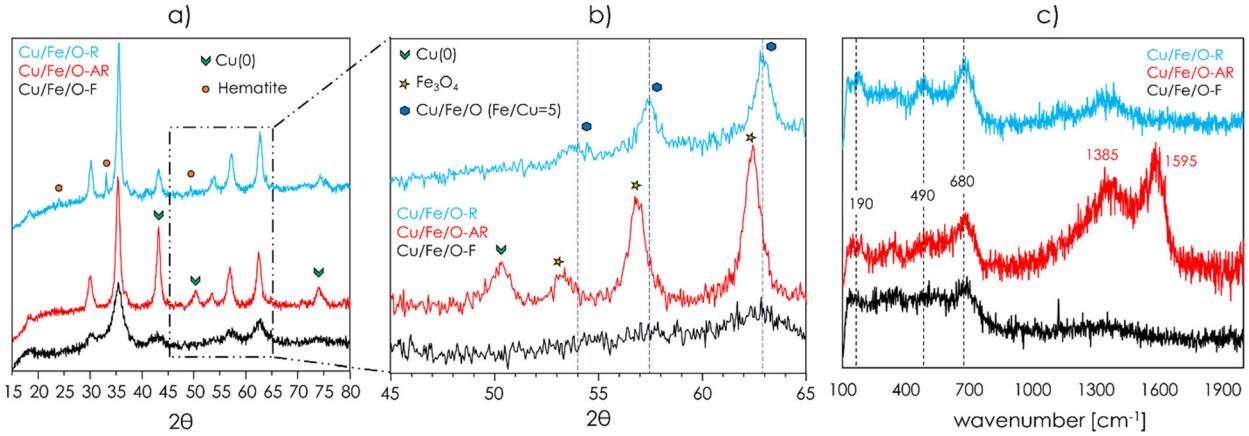

Fig. 4 a) and b) XRD powder patterns of Cu/Fe/O-F (fresh, black), Cu/Fe/O-AR (after reaction, red) and Cu/Fe/O-R (regenerated, light blue); c) Raman spectra (excitation source Ar^+ laser, 514.5 nm) of Cu/Fe/O-F (fresh, black), Cu/Fe/O-AR (after reaction, red) and Cu/Fe/O-R (regenerated, light blue).

respect to Cu/Fe/O-AR (Fig. 4b). However, a partial segregation of very small, well-dispersed, nanoparticles of CuO could not be excluded yet. Also, upon *in situ* regeneration a small fraction of the Fe-enriched spinel was oxidised to hematite and its crystallinity increased further (spinel CSD size = 15 nm, SSA = 55 $m^2\ g^{-1}$).

As mentioned previously, the reduction of Cu/Fe/O-F was investigated by means of TPR with H_2. The reduction profile (Fig. S14†) showed that the material was reduced in the same temperature range at which the ODH of isorosalva alcohol took place (*e.g.*, maximum of desorption centred at 295 °C). Moreover, the H_2 uptake (19.9 mL; 96 mL g^{-1}) calculated from the integrated area of the TPR profiles up to 450 °C corresponded to the amount required to obtain metallic Cu(0) and Fe_3O_4, in agreement with the outcome of the XRD characterization carried out over Cu/Fe/O-AR shown in Fig. 4a.

The Raman spectra of Cu/Fe/O-F, Cu/Fe/O-AR and Cu/Fe/O-R are reported in Fig. 4c. The spectrum of Cu/Fe/O-F was characterized by broad and poorly defined bands, with the most intense being centred at 680 cm^{-1} and corresponding to the A_{1g} vibrational mode of ferrite spinels.[81] The spectra of Cu/Fe/O-AR and Cu/Fe/O-R were more defined, owing to their higher crystallinity, and displayed also two bands centred at 490 cm^{-1} and 190 cm^{-1}, corresponding to the vibrational modes $F_{2g}(2)$ and $F_{2g}(1)$ respectively, in agreement with the results of Shebanova *et al.*[81] The presence of two strong bands centred at 1385 and 1595 cm^{-1} in the Raman spectrum of Cu/Fe/O-AR confirmed that during the ODH of IRA a certain amount of coke was formed over the catalyst surface, as suggested by the low C-balance obtained during the first 6 h of the catalytic tests shown in Fig. 3. The segregation of metallic Cu nanoparticles was clearly observed when high resolution TEM imaging was carried out over Cu/Fe/O-AR (Fig. 5), because the denser Cu appeared black or dark grey with respect to the light grey Fe-enriched spinel. Cu(0) segregated forming nanoparticles with a broad size distribution, ranging from a few nanometres to around 50 nm; the bigger nanoparticles were responsible for the diffraction peaks attributable to Cu(0) in the diffractogram of Cu/Fe/O-AR shown in Fig. 4a. An EDS microanalysis (shown in Fig. S15†) demonstrated that the black/dark grey nanoparticles contained mainly Cu (up to 78 atomic%), while the light grey nanoparticles were enriched in Fe (Fe/Cu atomic ratio = 12.9). The Fe-enriched spinel particles in Cu/Fe/O-AR maintained the quasi-spherical morphology of the parent Cu/Fe/O-F (see Fig. S8†) but their diameter increased from 5 to around 10 nm, in agreement with CSD sizes calculated from XRD. The high-resolution TEM characterization of Cu/Fe/O-R showed that after the *in situ* regeneration some nanoparticles were still present, suggesting that a fraction of the segregated Cu(0) in the parent Cu/Fe/O-AR was oxidised to CuO without being re-incorporated in the spinel structure of Cu/Fe/O. These

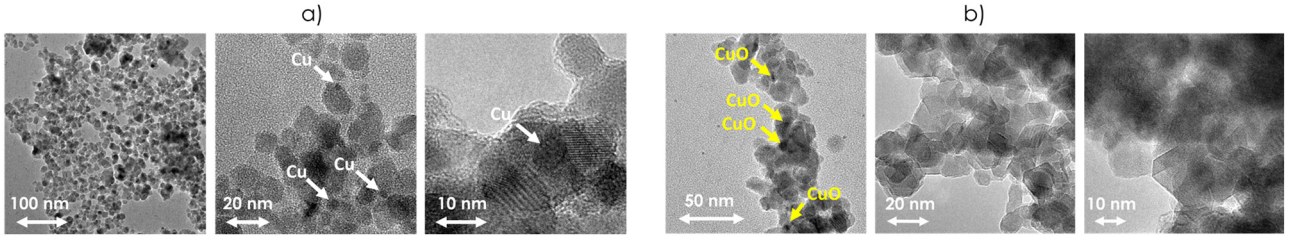

Fig. 5 High resolution TEM electron images of a) Cu/Fe/O-AR and b) Cu/Fe/O-R.

Open Access Article. Published on 04 janvris 2023. Downloaded on 16.07.2024 20:23:18.
This article is licensed under a Creative Commons Attribution-NonCommercial 3.0 Unported Licence.

nanoparticles of CuO were too small to be detected by means of XRD. Moreover, the light grey spinel particles became more crystalline, their average diameter increased further, and their quasi-spherical shape was lost in favour of a cubic morphology.

ODH of Isorosalva Alcohol over Cu-supported catalysts

The results reported in the previous section suggest that the Cu-ferrite can be considered a precursor of the real catalyst, which was made of small CuO nanoparticles supported over a Fe/Cu spinel, with the latter being formed upon a cycle of reactions followed by *in situ* regeneration. Starting from this hypothesis, a catalyst consisting of CuO supported over maghemite (CuO/γ-Fe_2O_3, 6 wt% of CuO) was prepared and its catalytic activity was compared to those of fresh Cu/Fe/O and two other materials containing only Fe (pure γ-Fe_2O_3) and only Cu (CuO/SiO_2, 6 wt% of CuO). The results of a catalyst screening carried out at 300 °C, τ = 1 s and with a feed consisting of IRA/O_2/N_2 = 5/5/90 mol% are reported in Fig. 6.

The activity of iron oxide alone (γ-Fe_2O_3) in the ODH of IRA to OPA was very low because the catalyst underwent a fast deactivation, leading to a negligible IRA conversion after only 4 h on stream, as shown in Fig. S16.† Its lack of activity has been attributed to the absence of Cu, meaning that its presence is crucial for the ODH reaction. The material containing only copper (CuO/SiO_2) performed poorly as well, displaying unsatisfactory activity and poor selectivity to OPA (*S* OPA = 24%, lower than that obtained with V_2O_5/TiO_2). Moreover, this catalyst fostered the dehydration of IRA to DD (*S* = 25%) and its consecutive cyclization to alkylated cyclic alkenes with 10 carbon atoms (CD, *S* = 9%) such as butyl-cyclohexene and pentyl-cyclopentene, as shown in Scheme S1 (ESI†). On the other hand, a remarkable cooperative effect between Cu and Fe occurred in the case of CuO/γ-Fe_2O_3, which displayed enhanced activity and improved selectivity with respect to both γ-Fe_2O_3 and CuO/SiO_2. This material also outperformed Cu/Fe/O: in fact, when Cu was supported over maghemite (CuO/γ-Fe_2O_3), the conversion of IRA was 33% (compared to 23 for the Cu/Fe/O catalyst), while OPA selectivity was 69% (compared to 51 for Cu/Fe/O); at the same time, the selectivity to CO_x decreased from 26 to 18% and the selectivity to other unknown compounds remained almost the same compared to Cu/Fe/O. Remarkably, this material was selective to OPA from the very beginning of the reaction, without the need for any "activation" procedure (Fig. S17†).

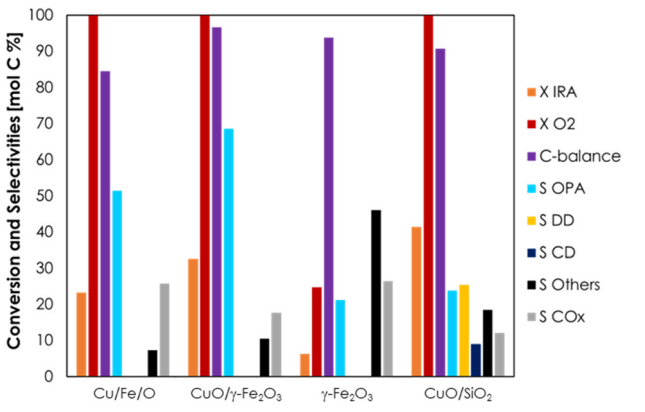

Fig. 6 ODH of IRA over Cu/Fe/O, CuO/γ-Fe_2O_3, γ-Fe_2O_3 and CuO/SiO_2. Reaction conditions: volume of catalyst = 1 cm^3, temperature = 300 °C, IRA/O_2/N_2 = 5/5/90 mol%, contact time (τ) = 1 second. Symbols: Isorosalva Alcohol conversion (*X* IRA, orange), oxygen conversion (*X* O_2, dark red) carbon balance (C-balance, purple), opalene selectivity (*S* OPA, light blue), decadiene selectivity (*S* DD, yellow), cyclic decene selectivity (*S* CD, dark blue), other by-products' selectivity (*S* Others, black) and CO_x selectivity (*S* CO_x, grey). Mean values calculated at the steady-state during the last 3 h of time on stream.

The synergistic effect between Cu and Fe observed for CuO/γ-Fe_2O_3 can be ascribed to the extremely high dispersion of Cu over the surface of maghemite as suggested by the TEM and EDS characterization (Fig. S9†). In fact, maghemite seemed to be capable of strongly bonding and stabilizing highly dispersed CuO-species (*e.g.*, small clusters or overlayers) or even incorporating Cu(II) into its lattice, possibly thanks to its surface defects and cationic vacancies.[82] As a consequence, both the conversion and the selectivity to OPA were improved, thanks to the formation of isolated active sites. A similar behaviour was observed for the regenerated, fully oxidized Cu/Fe/O-R catalyst, which was characterized by the presence of small nanoparticles of CuO dispersed over its surface, as shown by TEM characterization (Fig. 5b). However, this material displayed a transient activity with very high selectivity to total oxidation products during the first hour of reaction after regeneration (Fig. 3), which then dropped favouring the formation of OPA already during the second hour of reaction. In the literature it has been pointed out that in order to achieve high selectivity in partial oxidations with copper-based catalysts, CuO must be reduced to a certain extent in order to form isolated surface domains with a limited number of active lattice oxygen atoms, in agreement with the "site isolation" principle.[83] In line with this concept, some industrially relevant partial oxidations are carried out with catalysts containing Cu(0)[55] or Cu(I).[84] On the other hand, supported Cu(II)O is well known as a very active and selective catalyst for the total oxidation of methane[85] and VOCs (*e.g.*, toluene[86]), and high activities have been correlated with increasingly high dispersion of CuO on the support by several authors.[85,86] Hence, it is likely that the aforementioned change of selectivity of Cu/Fe/O-R from CO_2 (total oxidation) to OPA (selective partial oxidation, ODH) was due to the partial reduction of CuO nanoparticles to Cu(0). Although a similar behaviour might also be expected for CuO/γ-Fe_2O_3, it was not observed in the test reported in Fig. S17,† probably due to the higher dispersion of CuO-species and the lower Cu-loading (5 wt% expressed as metal) with respect to Cu/Fe/O (14.3 wt%).

Characterization of Cu-supported catalysts after reaction

A comparison between the XRD patterns before and after the ODH of IRA for CuO/SiO_2, γ-Fe_2O_3 and CuO/γ-Fe_2O_3 is reported in Fig. S18–S20,† respectively. The diffractogram of

 This journal is © The Royal Society of Chemistry 2023

Open Access Article. Published on 04 janvris 2023. Downloaded on 16.07.2024 20:23:18.
This article is licensed under a Creative Commons Attribution-NonCommercial 3.0 Unported Licence.

CuO/SiO_2 after reaction showed the superimposition of a broad band attributable to silica, the pattern of Cu(0) and that of Cu_2O, with no traces of the parent CuO; therefore, Cu(II) was completely reduced to Cu(I) and Cu(0) during the ODH of IRA. Unlike CuO/SiO_2, pure γ-Fe_2O_3 was not reduced during the reaction: in fact, except for the presence of a new set of weak reflections attributable to an impurity of hematite, its diffractogram after reaction was unaffected (Fig. S19b†). Therefore, the scarce activity of γ-Fe_2O_3 may be a consequence of its lack of reducibility in the reaction environment. Finally, in the diffractogram of CuO/γ-Fe_2O_3 after reaction all the reflections attributable to the spinel crystal structure of the support were shifted to lower 2θ values (Fig. S20b†), meaning that contrary to what happened with pure maghemite, in this case the γ-Fe_2O_3 support was reduced to magnetite (Fe_3O_4), very likely thanks to the presence of Cu.

The latter hypothesis was confirmed by means of TPR characterization of CuO/SiO_2, pure γ-Fe_2O_3 and CuO/γ-Fe_2O_3. The TPR profiles for these materials as well as a detailed discussion can be found in Fig. S21 and in Chapter S3 of the ESI† respectively. Briefly, the reduction of both CuO/SiO_2 and γ-Fe_2O_3 occurred in a single step, the former at a relatively low temperature (peak maximum at 316 °C) and the latter at higher temperatures (peak maximum at 450 °C, incomplete reduction). Meanwhile, the reduction profile of CuO/γ-Fe_2O_3 was characterized by two maxima centred at 322 °C (CuO) and 441 °C (γ-Fe_2O_3) respectively. However, the H_2 uptake calculated from the integrated area under the first peak centred at 322 °C was much higher than the one required to reduce all CuO to Cu(0), indicating that also a fraction of Fe(III), possibly the iron oxide support closer to the Cu(0)-species, was reduced at lower temperature. These results indicated that CuO was easily reduced at the temperature at which the ODH was investigated (300 °C) but the pure maghemite was not. However, the presence of supported Cu species in CuO/γ-Fe_2O_3 decreased the temperature needed for the reduction of the γ-Fe_2O_3 support to Fe_3O_4, making it feasible under the actual reaction conditions. These results confirmed the hypothesis of a synergy effect between the two metals, derived from the high dispersion of copper species over maghemite.

Conclusions

In this work the continuous-flow, gas-phase ODH of a mixture of decen-1-ol isomers ("Isorosalva", IRA) towards the corresponding mixture of aldehydes ("Opalene", OPA) has been reported for the first time.

The IRA mixture used in this study was produced and supplied by International Flavors & Fragrances Inc. and the target reaction was investigated in a conventional fixed-bed reactor over a novel, non-noble metal, Cu-ferrite catalyst ($Cu_{0.6}Fe_{2.4}O_{4.2}$, Cu/Fe/O) with spinel structure. This material displayed higher selectivity to OPA with respect to a traditional V_2O_5/TiO_2 catalyst (a benchmark catalyst for the ODH of light alcohols).

Increasing the contact time over the fresh Cu/Fe/O catalyst fostered several consecutive reactions such as OPA aldol condensation to form C_{20} branched aldehydes (ODT) and OPA overoxidation to decanoic acids followed by ketonization of the acids to C_{19} symmetric ketones (NDD).

However, it was found that OPA selectivity could be greatly increased up to 70% at 45% IRA conversion upon *in situ* regeneration of Cu/Fe/O with air at 400 °C for 3 h. This remarkable result was rationalized by characterizing in-depth the fresh, the spent and the regenerated catalyst. The combined results of XRD, BET, SEM-EDS, TEM and Raman spectroscopy showed that upon reaction the Cu-ferrite underwent a reduction to metallic Cu and a magnetite-like Fe-enriched spinel possessing a higher crystallinity with respect to the parent Cu-ferrite. Upon regeneration, not all the Cu was reincorporated into the Cu-ferrite structure; instead, it segregated forming small and well dispersed CuO nanoparticles over the surface of a Fe-enriched Cu-ferrite, which was the actual selective phase for OPA production.

Starting from these results, an *ad hoc* prepared catalyst based on 6 wt% of CuO supported on γ-Fe_2O_3 (maghemite) was prepared and subjected to comparative testing with 6 wt% CuO supported on SiO_2, pure maghemite γ-Fe_2O_3 and Cu/Fe/O. It was found that the performance of CuO/γ-Fe_2O_3 was superior to that of all the other materials both in terms of activity and selectivity. On the other hand, copper oxide alone (CuO/SiO_2) was not selective, while the iron oxide alone (γ-Fe_2O_3) was not active, hence the superior catalytic activity and selectivity of Cu/Fe/O and CuO/γ-Fe_2O_3 were attributed to a cooperative effect between Cu and Fe species.

Author contributions

Conceptualization: T. T., F. C. and P. R.; investigation: J. D. M. and F. O.; methodology: J. D. M. and T. T., writing-original draft: J. D. M. and T. T.; writing-review and editing: F. C., P. R., C. L. C.; Supervision: F. C. and C. L. C. Resources: C. L. C. All authors have read and agreed to the published version of the manuscript.

Conflicts of interest

There are no conflicts to declare.

Acknowledgements

IFF Benicarlò S. L. is acknowledged for funding and for the fruitful collaboration.

Notes and references

1 C. Lucarelli, A. Lolli, A. Giugni, L. Grazia, S. Albonetti, D. Monticelli and A. Vaccari, Efficient and ecofriendly route for the solvent-free synthesis of piperonal and aromatic

Open Access Article. Published on 04 janvris 2023. Downloaded on 16.07.2024 20:23:18.
This article is licensed under a Creative Commons Attribution-NonCommercial 3.0 Unported Licence.

aldehydes using Au/CeO2 catalyst, *Appl. Catal., B*, 2017, **203**, 314–323.
2 J. Panten and H. Sturburg, Flavors and fragrances, 2. Aliphatic compounds, in *Ullmann's Encyclopedia of Industrial Chemistry*, 2015, pp. 1–55.
3 C. Parmeggiani and F. Cardona, Transition metal based catalysts in the aerobic oxidation of alcohols, *Green Chem.*, 2012, **14**, 547–564.
4 I. Markò, A. Gautier, R. Dumeunier, K. Doda, F. Philippart, S. Brown and C. Urch, Efficient, copper-catalyzed, aerobic oxidation of primary alcohols, *Angew. Chem., Int. Ed.*, 2004, **43**, 1588–1591.
5 P. Gamez, I. Arends, R. Sheldon and J. Reedijk, Room temperature aerobic copper-catalysed selective oxidation of primary alcohols to aldehydes, *Adv. Synth. Catal.*, 2004, **346**, 805–811.
6 J. Hoover and S. Stahl, Highly practical copper(I)/TEMPO catalyst system for chemoselective aerobic oxidation of primary alcohols, *J. Am. Chem. Soc.*, 2011, **133**, 16901–16910.
7 A. Hanyu, E. Takezawa, S. Sakaguchi and Y. Ishii, Selective aerobic oxidation of primary alcohols catalyzed by a Ru(PPh3)3Cl2 / hydroquinone system, *Tetrahedron Lett.*, 1998, **39**, 5557–5560.
8 H. Mizoguchi, T. Uchida, K. Ishida and T. Katsuki, Ru(PPh3)(OH)-salen complex: a designer catalyst for chemoselective aerobic oxidation of primary alcohols, *Tetrahedron Lett.*, 2009, **50**, 3432–3435.
9 N. Komiya, T. Nakae, H. Sato and T. Naota, Water-soluble diruthenium complexes bearing acetate and carbonate bridges: highly efficient catalysts for aerobic oxidation of alcohols in water, *Chem. Commun.*, 2006, 4829–4831.
10 A. Dijksman, A. Marin-Gonzales, A. Mairata i Payeras, I. Arends and R. Sheldon, Efficient and selective aerobic oxidation of alcohols into aldehydes and ketones using ruthenium/TEMPO as the catalytic system, *J. Am. Chem. Soc.*, 2001, **123**, 6826–6833.
11 I. Markò, P. Giles, M. Tsukazaki, I. Chellè-Regnaut, C. Urch and S. Brown, Efficient, aerobic, ruthenium-catalyzed oxidation of alcohols into aldehydes and ketones, *J. Am. Chem. Soc.*, 1997, **119**, 12661–12662.
12 M. Hasan, M. Musawir, P. Davey and I. Kozhevnikov, Oxidation of primary alcohols to aldehydes with oxygen catalysed by tetra-n-propylammonium perruthenate, *J. Mol. Catal. A: Chem.*, 2002, **180**, 77–84.
13 M. Schultz, S. Hamilton, D. Jensen and M. Sigman, Development and comparison of the substrate scope of Pd-catalysts for the aerobic oxidation of alcohols, *J. Org. Chem.*, 2005, **70**, 3343–3352.
14 S. Gowrisankar, H. Neumann, D. Gordes, K. Thurow, H. Jiao and M. Beller, A convenient and selective palladium-catalyzed aerobic oxidation of alcohols, *Chem. – Eur. J.*, 2013, **19**, 15979–15984.
15 T. Nishimura, T. Onoue, K. Ohe and S. Uemura, Palladium(II)-catalyzed oxidation of alcohols to aldehydes and ketones by molecular oxygen, *J. Org. Chem.*, 1999, **64**, 6750–6755.
16 B. Guan, D. Xing, G. Cai, X. Wan, N. Yu, Z. Fang, L. Yang and Z. Shi, Highly selective aerobic oxidation of alcohol catalyzed by a gold(I) complex with an anionic ligand, *J. Am. Chem. Soc.*, 2005, **127**, 18004–18005.
17 X. Jiang, J. Liu and S. Ma, Iron-catalyzed aerobic oxidation of alcohols: lower cost and improved selectivity, *Org. Process Res. Dev.*, 2019, **23**, 825–835.
18 W. Yin, C. Chu, Q. Lu, J. Tao, X. Liang and R. Liu, Iron chloride/4-acetamido-TEMPO/sodium nitrite-catalyzed aerobic oxidation of primary alcohols to the aldehydes, *Adv. Synth. Catal.*, 2010, **352**, 113–118.
19 Y. Jing, J. Jiang, B. Yan, S. Lu, J. Jiai, H. Xue, G. Yang and G. Zheng, Activation of dioxygen by cobaloxime and nitric oxide for efficient TEMPO-catalyzed oxidation of alcohols, *Adv. Synth. Catal.*, 2011, **353**, 1146–1152.
20 R. Anderson, K. Griffin, P. Johnston and P. Alsters, Selective oxidation of alcohols to carbonyl compounds and carboxylic acids with platinum group metal catalysts, *Adv. Synth. Catal.*, 2003, **345**, 517–523.
21 N. Kakiuchi, Y. Maeda, T. Nishimura and S. Uemura, Pd(II)-hydrotalcite-catalyzed oxidation of alcohols to aldehydes and ketones using atmospheric pressure of air, *J. Org. Chem.*, 2001, **66**, 6620–6625.
22 E. Johnston, O. Verho, M. Karkas, M. Shakeri, C. Tai, P. Palmgren, K. Eriksson, S. Oscarsson and J. Backvall, Highly Dispersed Palladium Nanoparticles on Mesocellular Foam: An Efficient and Recyclable Heterogeneous Catalyst for Alcohol Oxidation, *Chem. – Eur. J.*, 2012, **18**, 12202–12206.
23 H. Wu, Q. Zhang and Y. Wang, Solvent-free aerobic oxidation of alcohols catalyzed by an efficient and recyclable palladium heterogeneous catalyst, *Adv. Synth. Catal.*, 2005, **347**, 1356–1360.
24 U. Pillai and E. Sahle-Demessie, Selective oxidation of alcohols by molecular oxygen over a Pd/MgO catalyst in the absence of any additives, *Green Chem.*, 2004, **6**, 161–165.
25 K. Yamaguchi, K. Mori, T. Mizugaki, K. Ebitani and K. Kaneda, Creation of a monomeric Ru species on the surface of hydroxyapatite as an efficient heterogeneous catalyst for aerobic alcohol oxidation, *J. Am. Chem. Soc.*, 2000, **122**, 7144–7145.
26 K. Yamaguchi and N. Mizuno, Supported ruthenium catalyst for the heterogeneous oxidation of alcohols with molecular oxygen, *Angew. Chem., Int. Ed.*, 2002, **41**, 4538–4542.
27 T. Stuchinskaya, M. Musawir, E. Kozhevnikova and I. Kozhevnikov, Liquid-phase oxidation of alcohols by oxygen and nitrous oxide catalysed by Ru-Co, *J. Catal.*, 2005, **231**, 41–47.
28 A. Bleloch, B. Johnson, S. Ley, A. Price, D. Shepard and A. Thomas, Modified mesoporous silicate MCM-41 materials: immobilised perruthenate - a new highly active heterogeneous oxidation catalyst for clean organic synthesis using molecular oxyge, *Chem. Commun.*, 1999, 1907–1908.
29 M. Beier, T. Hansen and J. Grunwaldt, Selective liquid-phase oxidation of alcohols catalyzed by a silver-based catalyst promoted by the presence of ceria, *J. Catal.*, 2009, **266**, 302–330.

 This journal is © The Royal Society of Chemistry 2023

Open Access Article. Published on 04 janvris 2023. Downloaded on 16.07.2024 20:23:18.
This article is licensed under a Creative Commons Attribution-NonCommercial 3.0 Unported Licence.

30 A. Abad, C. Almela, A. Corma and H. Garcia, Unique gold chemoselectivity for the aerobic oxidation of allylic alcohols, *Chem. Commun.*, 2006, 3178–3180.
31 V. Cortez Corberan, A. Gomez-Avilez, S. Martinez-Gonzalez, S. Ivanova, M. Dominguez and M. Gonzalez-Perewz, Heterogeneous selective oxidation of fatty alcohols: oxidation of 1-tetradecanol as a model substrate, *Catal. Today*, 2014, **238**, 49–53.
32 Y. Kotolevich, E. Kolobova, E. Khramov, M. Farias, Y. Zubavichus, H. Tiznado, S. Martinez-Gonzales, V. Cortes Corberan, J. Mota-Morales, A. Pestryakov and N. Bogdanchikova, n-Octanol oxidation on Au/TiO2 catalysts promoted with La and Ce oxides, *J. Mol. Catal. A: Chem.*, 2017, **427**, 1–10.
33 S. Reddy, S. Das and T. Punniyamurthy, Polyaniline supported vanadium catalyzed aerobic oxidation of alcohols to aldehydes and ketones, *Tetrahedron Lett.*, 2004, **45**, 3561–3564.
34 M. Musawir, P. Davey, G. Kelly and I. Kozhevnikov, Highly efficient liquid-phase oxidation of primary alcohols to aldehydes with oxygen catalysed by Ru–Co oxide, *Chem. Commun.*, 2003, 1414–1415.
35 T. Matsushita, K. Ebitani and K. Kaneda, Highly efficient oxidation of alcohols and aromatic compounds catalysed by the Ru-Co-Al hydrotalcite in the presence of molecular oxygen, *Chem. Commun.*, 1999, 265–266.
36 H. Ji, T. Mizugaki, K. Ebitani and K. Kaneda, Highly efficient oxidation of alcohols to carbonyl compounds in the presence of molecular oxygen using a novel heterogeneous ruthenium catalyst, *Tetrahedron Lett.*, 2002, **43**, 719–7183.
37 H. Ji, K. Ebitani, T. Mizugaki and K. Kaneda, Environmentally friendly alcohol oxidation using heterogeneous catalyst in the presence of air at room temperature, *Catal. Commun.*, 2002, **3**, 511–517.
38 H. Sun, Q. Hua, F.-f. Guo, Z. Wang and W. Huang, Selective aerobic oxidation of alcohols by using manganese oxide nanoparticles as an efficient heterogeneous catalyst, *Adv. Synth. Catal.*, 2012, **354**, 569–573.
39 T. Tabanelli, S. Passeri, S. Guidetti, F. Cavani, C. Lucarelli, F. Cargnoni and M. Mella, A cascade mechanism for a simple reaction: the gas-phase methylation of phenol with methanol, *J. Catal.*, 2019, **370**, 447–460.
40 N. Ballarini, F. Cavani, L. Maselli, A. Montaletti, S. Passeri, D. Scagliarini, C. Flego and C. Perego, The transformations involving methanol in the acid- and base-catalyzed gas-phase methylation of phenol, *J. Catal.*, 2007, **251**, 423–436.
41 V. Crocellà, G. Cerrato, G. Magnacca, C. Morterra, F. Cavani, S. Cocchi, S. Passeri, D. Scagliarini, C. Flego and C. Perego, The balance of acid, basic and redox sites in Mg/Me-mixed oxides: the effect on catalytic performance in the gas-phase alkylation of m-cresol with methanol, *J. Catal.*, 2010, **270**, 125–135.
42 T. Tabanelli, S. Cocchi, B. Gumina, L. Izzo, M. Mella, S. Passeri, F. Cavani, C. Lucarelli, J. Schutz, W. Bonrath and T. Netscher, Mg/Ga mixed-oxide catalysts for phenol methylation: outstanding performance in 2,4,6-trimethylphenol synthesis with co-feeding of water, *Appl. Catal., A*, 2018, **552**, 86–97.
43 J. De Maron, M. Eberle, F. Cavani, F. Basile, N. Dimitratos, P. Maireles-Torres, E. Rodriguez-Castellon and T. Tabanelli, Continuous-flow methyl methacrylate synthesis over gallium-based bifunctional catalysts, *ACS Sustainable Chem. Eng.*, 2021, **9**, 1790–1803.
44 A. Malmusi, J. Ochoa Velasquez, T. Tabanelli, F. Basile, C. Lucvarelli, S. Agnoli, F. Carraro, G. Granozzi and F. Cavani, Ethanol aerobic and anaerobic oxidation with FeVO4 and V2O5 catalysts, *Appl. Catal., A*, 2019, **570**, 139–147.
45 M. Crivello, C. Perez, S. Mendieta, S. Casuscelli, G. Eimer, V. Elias and E. Herrero, n-Octyl alcohol dehydrogenation over copper catalysts, *Catal. Today*, 2008, **133–135**, 787–792.
46 D. Sun, T. Misu, Y. Yamada and S. Sato, Advantages of using Cu/SiO2 catalyst for vapor-phase dehydrogenation of 1-decanol into decanal, *Appl. Catal., A*, 2019, **582**, 117109.
47 L. Izzo, T. Tabanelli, F. Cavani, P. Vasquez Blair, C. Lucarelli and M. Mella, The competition between dehydrogenation and dehydration reactions for primary and secondary alcohols over gallia: unravelling the effects of molecular and electronic structure via a two-pronged theoretical/experimental approach, *Catal. Sci. Technol.*, 2020, **10**, 3433–3449.
48 L. Grazia, A. Lolli, F. Folco, Y. Zhang, S. Albonetti and F. Cavani, Gas-phase cascade upgrading of furfural to 2-methylfuran using methanol as a H-transfer reactant and MgO based catalysts, *Catal. Sci. Technol.*, 2016, **6**, 4418–4427.
49 L. Grazia, D. Bonincontro, A. Lolli, T. Tabanelli, C. Lucarelli, S. Albonetti and F. Cavani, Exploiting H-transfer as a tool for the catalytic reduction of bio-based building blocks: the gas-phase production of 2-methylfurfural using a FeVO4 catalyst, *Green Chem.*, 2017, **19**, 4412–4422.
50 A. Nagy and G. Mestl, High temperature partial oxidation reactions over silver catalysts, *Appl. Catal., A*, 1999, **188**, 337–353.
51 V. Folliard, G. Postole, L. Marra, J. Dubois and A. Aroux, Sustainable acrolein production from bio-alcohols on spinel catalysts: Influence of magnesium substitution by various transition metals (Fe, Zn, Co, Cu, Mn), *Appl. Catal., A*, 2020, **608**, 117871.
52 A. Chieregato, J. L. Nieto and F. Cavani, Mixed-oxide catalysts with vanadium as the key element for gas-phase reactions, *Coord. Chem. Rev.*, 2015, **301–302**, 3–23.
53 G. Reuss, W. Disteldorf, A. Gamer and A. Hilt, Formaldehyde, *Ullmann's Encycl. Ind. Chem.*, 2000, vol. 15, pp. 735–768.
54 M. Eckert, G. Fleischmann, J. Reinhard, H. Bolt and K. Golka, Acetaldehyde, *Ullmann's Encycl. Ind. Chem.*, 2012, vol. 1, pp. 191–207.
55 W. Aquila, H. Fuchs, O. Worz, W. Ruppel and K. Halbritter, Continous industrial production of unsaturated aliphatic aldehydes in a tube bundle reactor. Brevetto US6013843A, 2000.

Open Access Article. Published on 04 janvris 2023. Downloaded on 16.07.2024 20:23:18.
This article is licensed under a Creative Commons Attribution-NonCommercial 3.0 Unported Licence.

56 S. Biella and M. Rossi, Gas phase oxidation of alcohols to aldehydes or ketones catalysed by supported gold, *Chem. Commun.*, 2003, 378–379.
57 W. Yi, W. Yuan, Y. Meng, S. Zou, Y. Zhou, W. Hong, J. Che, M. Hao, B. Ye, L. Xiao, Y. Wang, H. Kobayashi and J. Fan, A rational solid-State synthesis of supported Au–Ni bimetallic nanoparticles with enhanced activity for gas-phase selective oxidation of alcohols, *ACS Appl. Mater. Interfaces*, 2017, **9**, 31853–31860.
58 G. Zhao, H. Hu, M. Deng, M. Ling and Y. Lu, Au/Cu-fiber catalyst with enhanced low-temperature activity and heat transfer for the gas-phase oxidation of alcohols, *Green Chem.*, 2011, **13**, 55–58.
59 I.-D. Huang, L. Polinski and K. Rao, Oxidative dehydrogenation of alcohols to aldehydes and ketones, Brevetto US4154762, 1979.
60 G. Zhao, M. Deng, Y. Jiang, H. Hu, J. Huang and Y. Lu, Microstructured Au/Ni-fiber catalyst: galvanic reaction preparation and catalytic performance for low-temperature gas-phase alcohol oxidation, *J. Catal.*, 2013, **301**, 46–53.
61 Z. Yang, J. Li, X. Yang, X. Xie and Y. Wu, Gas-phase oxidation of alcohols over silver: The extension of catalytic cycles of oxidation of alcohols in the liquid-phase, *J. Mol. Catal. A: Chem.*, 2005, **241**, 15–22.
62 J. Shen, W. Shan, Y. Zhang, J. Du, H. Xu, K. Fan, W. Shen and Y. Tang, Gas-phase selective oxidation of alcohols: in situ electrolytic nano-silver/zeolite film/copper grid catalyst, *J. Catal.*, 2006, **237**, 94–101.
63 C. Zhang, P. Chen, J. Liu, Y. Zhang, W. Shen, H. Xu and Y. Tang, Ag microparticles embedded in Si nanowire arrays: a novel catalyst for gas-phase oxidation of high alcohol to aldehyde, *Chem. Commun.*, 2008, 3290–3292.
64 L. Zhao, L. Kong, C. Liu, Y. Wang and L. Dai, AgCu/SiC-powder: a highly stable and active catalyst for gas-phase selective oxidation of alcohols, *Catal. Commun.*, 2017, **98**, 1–4.
65 P. Gallezot, L. Ceroni and A. Perrard, Oxidative dehydrogenation of rosalva to costenal on supported silver catalyst, *J. Mol. Catal. A: Chem.*, 1998, **129**, L127–L130.
66 A. Narula, E. Arruda and F. Schiet, Decenal mixtures and their use in perfume composition, Brevetto US8461100B1, 2013.
67 F. Huang, Y. Zhang, Y. Yao, W. Yang and Y. Tao, Synthesis of (4E,6Z,10Z)-hexadeca-4,6,10-trien-1-ol and (4E,6E,10Z)-hexadeca-4,6,10-trien-1-ol, the pheromone components of cocoa pod borer moth Conopomorpha cramerella, *RSC Adv.*, 2017, **57**, 35575–35580.
68 K. Lorber, G. Zeh, J. Regler and A. Buettner, Structure-odor relationships of (Z)-3-alken-1-ols, (Z)-3-alkenals, and (Z)-3-alkenoic acids, *J. Agric. Food Chem.*, 2018, **66**, 2334–2343.
69 E. Brodl, J. Ivkovic, C. Tabib, R. Breinbauer and P. Macheroux, Synthesis of α,β-unsaturated aldehydes as potential substrates for bacterial luciferases, *Bioorg. Med. Chem.*, 2017, **25**, 1487–1495.
70 Y. Shigekazu and Y. Yasuyuki, Nickel-catalyzed oxidation of allylic alcohols with K2S2O8, *Chem. Lett.*, 1989, **18**, 1361–1364.
71 C. Wulkesch and C. Czekelius, Straightforward synthesis of fluorinated enals via photocatalytic α-perfluoroalkenylation of aldehydes, *J. Org. Chem.*, 2021, **86**, 7425–7438.
72 E. Cao, I. Zuburtikudis, N. Al-Rifay, M. Roydhouse and A. Gavriilidis, Enhanced performance of oxidation of rosalva (9-decen-1-ol) to costenal (9-decenal) on porous silicon-supported silver catalyst in a microstructured reactor, *Processes*, 2014, **2**, 141–157.
73 C. Trevisanut, O. Vozniuk, M. Mari, S. Arenas Urrea, C. Lorentz, J.-M. Millet and F. Cavani, The chemical-loop reforming of alcohols on spinel-type mixed oxides: comparing Ni, Co, and Fe ferrite vs magnetite performances, *Top. Catal.*, 2016, **59**, 1600–1613.
74 F. Folco, J. Velasquez Ochoa, F. Cavani, L. Ott and M. Janssen, Ethanol gas-phase ammoxidation to acetonitrile: the reactivity of supported vanadium oxide catalysts, *Catal. Sci. Technol.*, 2017, **7**, 200–212.
75 W. Zhang, G. Innocenti, M. Ferbinteanu, E. Ramos-Fernandez, A. Sepulveda-Escribano, H. Wu, F. Cavani, G. Rothemberg and R. Shiju, Understanding the oxidative dehydrogenation of ethyl lactate to ethyl pyruvate over vanadia/titania, *Catal. Sci. Technol.*, 2018, **8**, 3707–3978.
76 D. Maity and D. Agrawal, Synthesis of iron oxide nanoparticles under oxidizing environment and their stabilization in aqueous and non-aqueous media, *J. Magn. Magn. Mater.*, 2007, **308**, 46–55.
77 W. Wang, Q. Zhou, X. Fei, Y. He, P. Zhang, G. Zhang, L. Peng and W. Xie, Synthesis of CuO nano- and micro-structures and their Raman spectroscopic studies, *CrystEngComm*, 2010, **12**, 2232–2237.
78 C. Bandinelli, B. Lambiase, T. Tabanelli, J. De Maron, N. Dimitratos, F. Basile, P. Concepcion, N. J. Lopez and F. Cavani, A study of the oxidehydration of 1,2-propanediol to propanoic acid with bifunctional catalysts, *Appl. Catal., A*, 2019, **582**, 117102.
79 A. Vassoi, T. Tabanelli, A. Sacchetti, F. Di Gioia, L. Capuzzi and F. Cavani, The oxidative cleavage of 9,10-dihydroxystearic triglyceride with oxygen and Cu oxide-based heterogeneous catalysts, *ChemSusChem*, 2021, **14**, 2375–2382.
80 J. De Maron, L. Bellotti, A. Baldelli, A. Fasolini, N. Schiaroli, C. Lucarelli, F. Cavani and T. Tabanelli, Evaluation of the catalytic activity of metal phosphates and related oxides in the ketonization of propionic acid, *Sustainable Chem.*, 2022, **3**, 58–75.
81 O. Shebanova and P. Lazor, Raman spectroscopic study of magnetite (FeFe2O4): a new assignment for the vibrational spectrum, *J. Solid State Chem.*, 2003, **174**, 424–430.
82 R. Vandenberghe, E. De Grave, C. Landuydt and L. Bowen, Some aspect conceriìning the characterization of iron oxides and hydroxides in soils and clays, *Hyperfine Interact.*, 1990, **53**, 175–196.
83 R. Grasselli, Site isolation and phase cooperation: two important concepts in selective oxidation catalysis: a retrospective, *Catal. Today*, 2014, **238**, 10–27.

 This journal is © The Royal Society of Chemistry 2023

Open Access Article. Published on 04 janvris 2023. Downloaded on 16.07.2024 20:23:18.
This article is licensed under a Creative Commons Attribution-NonCommercial 3.0 Unported Licence.

84 G. Hearne and M. Adams, Production of unsaturated carbonilic compounds, Brevetto US2451485, 1947.
85 M. Marion, E. Garbowski and M. Primet, Physicochemical Properties of Copper Oxide Loaded Alumina in Methane Combustion, *J. Chem. Soc., Faraday Trans.*, 1990, **86**, 3027–3032.
86 P. Larsson, A. Andersson, L. Wallenberg and B. Svensson, Combustion of CO and toluene; characterisation of copper oxide supported on titania and activity comparisons with supported cobalt, iron, and manganese oxide, *J. Catal.*, 1996, **163**, 279–293.